

## Evolution of flux ropes in the magnetotail: A three-dimensional global hybrid simulation

S. Lu, Y. Lin, Q. M. Lu, X. Y. Wang, R. S. Wang, C. Huang, M. Y. Wu, and S. Wang

Citation: *Physics of Plasmas* (1994-present) **22**, 052901 (2015); doi: 10.1063/1.4919615

View online: <http://dx.doi.org/10.1063/1.4919615>

View Table of Contents: <http://scitation.aip.org/content/aip/journal/pop/22/5?ver=pdfcov>

Published by the [AIP Publishing](#)

---

### Articles you may be interested in

[The relation between reconnected flux, the parallel electric field, and the reconnection rate in a three-dimensional kinetic simulation of magnetic reconnection](#)

*Phys. Plasmas* **20**, 122105 (2013); 10.1063/1.4833675

[Gyrokinetic simulations of magnetic reconnection](#)

*Phys. Plasmas* **18**, 112102 (2011); 10.1063/1.3656965

[Defining and identifying three-dimensional magnetic reconnection in resistive magnetohydrodynamic simulations of Earth's magnetosphere](#)

*Phys. Plasmas* **15**, 056504 (2008); 10.1063/1.2913548

[Development and anisotropy of three-dimensional turbulence in a current sheet](#)

*Phys. Plasmas* **14**, 062304 (2007); 10.1063/1.2743518

[Current sheet formation and nonideal behavior at three-dimensional magnetic null points](#)

*Phys. Plasmas* **14**, 052106 (2007); 10.1063/1.2722300

---

Did your publisher get  
**18 MILLION DOWNLOADS** in 2014?  
AIP Publishing did.



THERE'S POWER IN NUMBERS. Reach the world with AIP Publishing.



# Evolution of flux ropes in the magnetotail: A three-dimensional global hybrid simulation

S. Lu,<sup>1,2</sup> Y. Lin,<sup>3</sup> Q. M. Lu,<sup>1,a)</sup> X. Y. Wang,<sup>3</sup> R. S. Wang,<sup>4</sup> C. Huang,<sup>1</sup> M. Y. Wu,<sup>1</sup> and S. Wang<sup>1</sup>

<sup>1</sup>CAS Key Laboratory of Geospace Environment, Department of Geophysics and Planetary Sciences, University of Science and Technology of China, Hefei, China

<sup>2</sup>State Key Laboratory of Space Weather, National Space Science Center, Chinese Academy of Sciences, Beijing, China

<sup>3</sup>Physics Department, Auburn University, Auburn, Alabama, USA

<sup>4</sup>Key Laboratory of Earth and Planetary Physics, Institute of Geology and Geophysics, Chinese Academy of Sciences, Beijing, China

(Received 3 February 2015; accepted 17 April 2015; published online 4 May 2015)

Flux ropes in the Earth's magnetotail are widely believed to play a crucial role in energy transport during substorms and the generation of energetic particles. Previous kinetic simulations are limited to the local-scale regime, and thus cannot be used to study the structure associated with the geomagnetic field and the global-scale evolution of the flux ropes. Here, the evolution of flux ropes in the magnetotail under a steady southward interplanetary magnetic field are studied with a newly developed three-dimensional global hybrid simulation model for dynamics ranging from the ion Larmor radius to the global convection time scales. Magnetic reconnection with multiple X-lines is found to take place in the near-tail current sheet at geocentric solar magnetospheric distances  $x = -30R_E \sim -15R_E$  around the equatorial plane ( $z = 0$ ). The magnetotail reconnection layer is turbulent, with a nonuniform structure and unsteady evolution, and exhibits properties of typical collisionless fast reconnection with the Hall effect. A number of small-scale flux ropes are generated through the multiple X-line reconnection. The diameter of the flux ropes is several  $R_E$ , and the spatial scale of the flux ropes in the dawn-dusk direction is on the order of several  $R_E$  and does not extend across the entire section of the magnetotail, contrary to previous models and MHD simulation results and showing the importance of the three-dimensional effects. The nonuniform and unsteady multiple X-line reconnection with particle kinetic effects leads to various kinds of flux rope evolution: The small-scale flux ropes propagate earthward or tailward after formation, and eventually merge into the near-Earth region or the mid-/distant-tail plasmoid, respectively. During the propagation, some of the flux ropes can be tilted in the geocentric solar magnetospheric ( $x, y$ ) plane with respect to the  $y$  (dawn-dusk) axis. Coalescence between flux ropes is also observed. At the same time, the evolution of the flux ropes in the multiple X-line reconnection layer can also lead to the acceleration and heating of ions. © 2015 AIP Publishing LLC. [<http://dx.doi.org/10.1063/1.4919615>]

## I. INTRODUCTION

Flux ropes, three-dimensional (3-D) helical magnetic structures generated during magnetic reconnection,<sup>1–6</sup> are believed to play a critical role in energy transport during substorms,<sup>7</sup> and they are also considered to be responsible for the generation of energetic particles in the magnetotail.<sup>8–13</sup> Flux ropes were believed to be driven only tailward by the pressure gradient and magnetic tension forces at the early stage when the concept was first put forward.<sup>14</sup> However, observations of both tailward and earthward propagating flux ropes in the magnetotail were later reported,<sup>15,16</sup> resulting in an extension of the plasmoid model of substorms. On the basis of Geotail observations, Slavin *et al.*<sup>17</sup> further studied flux ropes in the magnetotail, and termed the tailward propagating flux ropes “plasmoid-type” and the earthward propagating flux ropes

“bursty bulk flow (BBF)-type.” The earthward moving (BBF-type) flux ropes have also been observed by other spacecraft, such as Cluster<sup>18,19</sup> and THEMIS.<sup>20</sup>

Magnetic reconnection at multiple X-lines is widely believed to be responsible for the formation of flux ropes in a plasma sheet.<sup>17,21,22</sup> Two-dimensional (2-D) particle-in-cell and hybrid simulations have been performed to study magnetic reconnection and the associated flux ropes (usually called magnetic islands in the 2-D regime). The structure of the reconnection region was found to be determined by the ion kinetic physics,<sup>23–26</sup> and the generation mechanism of the core field in the flux ropes was also investigated.<sup>27–29</sup> However, these studies considered only the physics of a local Harris current sheet. Lin and Swift<sup>30</sup> carried out a 2-D global hybrid simulation to study the evolution of the near-Earth plasma sheet, and showed that reconnection X-lines and flux ropes/plasmoids can be generated by diverging flows in the plasma sheet. The evolution of flux ropes was also studied with 3-D particle-in-cell simulations. Daughton *et al.*<sup>31,32</sup>

<sup>a)</sup> Author to whom correspondence should be addressed. Electronic mail: qmlu@ustc.edu.cn

showed that, for the common type of reconnection layer, the 3-D evolution is dominated by the formation and interaction of helical magnetic flux ropes in the electron layer. New flux ropes spontaneously appear, leading to a turbulent reconnection layer.

However, most of the aforementioned simulation studies were limited to the local-scale regime, in which the structure associated with the geomagnetic field and the global-scale evolution of the flux ropes cannot be studied. Using the configuration of the Earth's magnetosphere, 3-D global-scale magnetohydrodynamic (MHD) simulations have been performed to investigate the flux ropes/plasmoids associated with the magnetotail reconnection.<sup>33–40</sup> The 3-D global MHD simulations show the occurrence of the near-tail reconnection under the southward interplanetary magnetic field (IMF). Large-scale flux ropes/plasmoids form in the mid-tail by magnetic reconnection<sup>33–36</sup> and then move tailward.<sup>37–39</sup> Winglee *et al.*<sup>40</sup> also investigated the evolution of flux ropes during substorm processes with a multi-fluid MHD model,<sup>41</sup> and identified both earthward and tailward moving flux ropes in the simulations.

The spatial scale of the flux ropes/plasmoids in MHD simulations is usually on the order of several tens of  $R_E$  in both the  $x$  and  $y$  directions of the geocentric solar magnetospheric (GSM) coordinate system, and such large-scale flux ropes/plasmoids are observed in the distant-tail.<sup>42</sup> However, small-scale flux ropes with a spatial scale of several  $R_E$  have also been identified and investigated with Geotail observations.<sup>17,43</sup> The MHD models, which are limited to spatial and temporal scales that are much larger than the particle kinetic scales, have limitations in the description of these small-scale flux ropes. Therefore, for a better understanding of the 3-D physics of the flux ropes in the Earth's magnetotail, it is necessary to include both the realistic global-scale configuration of the magnetosphere and the small-scale particle kinetic effects.

In this paper, a newly developed 3-D global-scale hybrid simulation model, with a domain including both the dayside and nightside magnetosphere, is used to investigate the dynamic processes in the magnetotail under a southward IMF. In our previous study,<sup>44</sup> we investigated several important processes associated with substorms such as dipolarization, ballooning instability, and ion injection. In the present study, we mainly focus on the physics of the flux ropes and magnetotail reconnection. Our simulation results show that a number of small-scale (several  $R_E$  in the GSM  $x$  and  $y$  directions) flux ropes are generated during the fast reconnection in the magnetotail that possesses multiple X-lines. The particle kinetic effects lead to various kinds of flux rope evolution, such as earthward/tailward propagation, tilt in the GSM ( $x, y$ ) plane with respect to the  $y$  axis, merging, and coalescence. The evolution of the flux ropes in the magnetotail reconnection layer, on the other hand, can also lead to the acceleration and heating of the ions. The remainder of the paper is as follows. Section II describes the simulation model. Section III presents the simulation results, and Sec. IV presents the summary and discussions.

## II. SIMULATION MODEL

The 3-D global hybrid simulation model used in this study is developed by extending a previous version of the model that contains only the dayside magnetosphere<sup>45</sup> to include the nightside. The simulation scheme is described by Swift<sup>46</sup> in detail. In the hybrid code, the ions (protons) are treated as discrete, fully kinetic particles, and the electrons are treated as a massless fluid.

The equation for ion particle motion, in the simulation units, is given by

$$\frac{d\mathbf{v}_p}{dt} = \mathbf{E} + \mathbf{v}_p \times \mathbf{B} - \nu(\mathbf{V}_p - \mathbf{V}_e), \quad (1)$$

where  $\mathbf{v}_p$  is the ion particle velocity,  $\mathbf{E}$  is the electric field,  $\mathbf{B}$  is the magnetic field, and  $\mathbf{V}_p$  and  $\mathbf{V}_e$  are the bulk flow velocities of ions and electrons, respectively. A small current-dependent collision frequency,  $\nu \approx 0.01\Omega j/j_0$ , is imposed to simulate the anomalous resistivity and trigger magnetic reconnection in the simulation (here  $\Omega$  is the local ion gyrofrequency,  $j_0 = B_0/\mu_0 d_{i0}$ , and  $d_{i0} = c/\omega_{pi0}$  is the ion inertial length of the solar wind).

In the region  $r < 6R_E$ , the fluid approximation is used to simulate the cold and dense plasma in the inner magnetosphere. The ion fluid density is given as

$$N_f = (N_{eq}/r^3)/[1 - \tanh(r - 6.5)], \quad (2)$$

where  $N_{eq} = 1000 \text{ cm}^{-3}$  and  $r$  has a unit of  $R_E$ .

The electron fluid momentum equation

$$\mathbf{E} = -\mathbf{V}_e \times \mathbf{B} - \nu(\mathbf{V}_e - \mathbf{V}_i) - \frac{1}{N} \nabla p_e \quad (3)$$

is used to calculate the electric field, where  $N = N_p + N_f$  is the total ion number density,  $N_p$  is the number density of discrete ions,  $\mathbf{V}_i = \frac{N_p}{N} \mathbf{V}_p + \frac{N_f}{N} \mathbf{V}_f$  is the total ion bulk velocity, and  $p_e = NT_e$  is the electron pressure. In the hybrid code, uniform electron temperature  $T_e$  is adopted for simplicity.

The electron flow speed is evaluated from Ampere's Law

$$\mathbf{V}_e = \mathbf{V}_i - \frac{\nabla \times \mathbf{B}}{\alpha N}, \quad (4)$$

where in the simulation units,  $\alpha = 4\pi e^2/m_i c^2$ ,  $e$  is the electron charge, and  $m_i$  is the ion mass. Note that  $(\alpha N)^{-1/2}$  is the ion inertial length. The magnetic field is advanced in time by Faraday's law

$$\frac{\partial \mathbf{B}}{\partial t} = -\nabla \times \mathbf{E}. \quad (5)$$

The numerical scheme is accurate to second order in both space and time. The subcycle time scheme is used to advance the magnetic field, which maintains the numerical stability in the dipole high-field region and saves considerable computation time. The simulation is performed with a massively parallel computation.

The simulation is carried out in a cuboid domain in the GSM coordinate system, from  $x = -60R_E$  on the nightside

to  $x = 20R_E$  on the dayside,  $y = -30R_E$  to  $30R_E$  in the dawn-dusk direction, and  $z = -30R_E$  to  $30R_E$  in the north-south direction. An inner boundary is assumed at a geocentric distance of  $r \approx 3.5R_E$ . The computation uses a Cartesian coordinate system, in which the inner boundary is composed of a zig-zag grid line approximating the spherical surface. Nonuniform Cartesian cell grids are adopted, with a resolution of  $\Delta x = \Delta y = \Delta z = 0.15R_E$  in the near-Earth magnetotail and a lower resolution in the lobes. High grid resolution,  $0.09R_E$ , is adopted in the vicinity of the dayside magnetopause; nevertheless, the kinetic physics of magnetic reconnection in the dayside magnetopause may still not be resolved completely. However, these effects of the dayside kinetic structures, which are not likely to dramatically affect the kinetic physics in the magnetotail, are not emphasized in the present study. The cell dimensions are  $n_x \times n_y \times n_z = 373 \times 217 \times 217$ . More than  $3 \times 10^9$  particles are employed to simulate the plasma. The typical time step is  $\Delta t = 0.05\Omega_0^{-1}$ .

Initially, a geomagnetic dipole field plus an image dipole is adopted for  $x < 15R_E$ , and a uniform solar wind with the IMF  $B_0$  of  $B_{x0} = B_{y0} = 0$  and  $B_{z0} = -10$  nT is imposed for  $x > 15R_E$ . The corresponding solar wind ion gyrofrequency is  $\Omega_0 = 0.958$  s $^{-1}$ . The solar wind ion number density is  $N_0 = 6$  cm $^{-3}$ , and the solar wind Alfvén speed is thus  $V_{A0} = 89$  km/s. The solar wind convection speed is set to  $V_0 = 700$  km/s, the ion temperature is  $T_{i0} = 10$  eV, and the electron-to-ion temperature ratio is  $T_{e0}/T_{i0} = 0.1$ . Initially, in the dipole field region, the ion particle density is  $0.05N_0$ . The magnetosphere forms self-consistently through the interaction between the solar wind and geomagnetic field. The solar wind flows along the  $-x$  direction from the dayside boundary at  $x = 20R_E$ , carrying the steady IMF. Open boundary conditions are used for the five remaining boundaries at  $x = -60R_E$ ,  $y = \pm 30R_E$ , and  $z = \pm 30R_E$ . The inclusion of the cold ion fluid in the inner magnetosphere simplifies the conditions for a fluid-dominant, low-altitude, inner boundary. A combination of spherical and Cartesian coordinates is used at the inner boundary. We let particles be reflected at  $r = 3.5R_E$ . The electric and magnetic fields at the boundary reside on the Cartesian boundary approximating a spherical boundary, and are extrapolated to an extra grid point inside the  $r = 3.5R_E$  surface. The magnetic field is assumed to maintain the dipole field values at the inner boundary. A magnetospheric-ionospheric electrostatic coupling model is incorporated into the hybrid model to drive the inner magnetospheric convection, as in existing global MHD models.<sup>36,47</sup> The field-aligned currents, calculated within the inner boundary, are mapped along the geomagnetic field lines into the ionosphere as input to the ionospheric potential equation

$$\nabla \cdot \left( -\sum \cdot \nabla \Phi \right) = J_{\parallel} \sin I, \quad (6)$$

where  $\sum$  is the conductance tensor,  $\Phi$  is the electric potential,  $J_{\parallel}$  is the field-aligned current density, and  $I$  is the inclination of the dipole field at the ionosphere. In this paper, uniform Pederson conductance  $\sum_p = 5$  (Siemens) is adopted, and the Hall conductance  $\sum_H$  is assumed to be zero.

To accommodate the available computing resources, a larger-than-realistic solar wind ion inertial length  $d_{i0} = 0.1R_E$  is chosen in this study. Given that the peak ion number density in the plasma sheet is on the order of  $0.1N_0$ ,<sup>48</sup> the ion inertial length in the magnetotail is around  $0.25R_E \sim 0.55R_E$  in the simulation. Hybrid simulations resolve the kinetic physics above the spatial scale of the ion inertial length, with  $kd_i \sim 1$ . Therefore, our grid size,  $\Delta x = \Delta y = \Delta z = 0.15R_E$ , is sufficient to resolve the ion kinetic physics, as seen in previous hybrid simulations.<sup>24-27</sup> Owing to the artificiality of the solar wind inertial length, a scaling factor is necessary. For a typical solar wind density of  $6$  cm $^{-3}$ , the realistic solar wind ion inertial length is  $0.0148R_E$ . Given that the length  $d_{i0}$  chosen in the simulation is a factor of 6.77 larger than that in reality, there is a scaling factor of 6.77 in the conversion of the length scales from the simulation to reality. The global convection time scale is therefore also larger by the same factor. In the hybrid simulation, the magnetic field is normalized to IMF  $B_0$ , time to  $\Omega_0^{-1}$ , the spatial length to  $d_{i0}$ , and thus, the velocity to the solar wind Alfvén speed  $V_{A0}$  correspondingly. Nevertheless, to make a direct comparison with the global convection time scales in reality, we scale back the time by a factor of 6.77 to fit in the real convection times. To make a direct comparison with the realistic Earth's magnetosphere, in the presentation below, the spatial length has a unit of  $R_E$ , and the velocity units of km/s. The magnetic field has the unit nT, the temperature the unit eV, and the ion number density the unit cm $^{-3}$ .

### III. SIMULATION RESULTS

#### A. Magnetotail reconnection and flux ropes

Figure 1 shows a 3-D perspective of the magnetic field lines and contours of the ion density  $N$  in the equatorial ( $z = 0$ ) and noon-midnight meridian ( $y = 0$ ) planes at  $t =$ (a) 1437 s, (b) 1788 s, and (c) 2016 s. The blue magnetic field lines represent the southward IMF in the solar wind and magnetosheath, while the red magnetic field lines represent the geomagnetic field. Southward magnetosheath field lines are reconnected with the northward geomagnetic field at the dayside magnetopause. The solar wind plasma, energy, and magnetic flux thus penetrate through the magnetopause and are transported tailward via magnetospheric convection, which results in a long (in the  $x$  direction) and thin current sheet in the magnetotail. At  $t = 1437$  s, before the occurrence of the magnetotail reconnection, the standoff distance of the bow shock is about  $11.5R_E$  along the Sun-Earth line, and the subsolar distance of the magnetopause is about  $7.5R_E$ . With the accumulation of the magnetic flux and energy in the magnetotail, the current sheet becomes thinner and thinner. At  $t = 1788$  s, magnetic reconnection occurs around  $x = -18R_E$ , where the magnetotail current sheet is thinnest. From the ion density distribution, we note that some of the plasma in the near-tail region is injected into the inner magnetosphere because of the magnetotail reconnection and related processes, and the ion density in the inner magnetosphere thus is about twice that before the magnetotail reconnection occurs. As the magnetotail reconnection proceeds with multiple X-lines, at  $t = 2016$  s, a number of small-scale, 3-D flux ropes form in the equatorial plane from  $x = -30R_E$  to

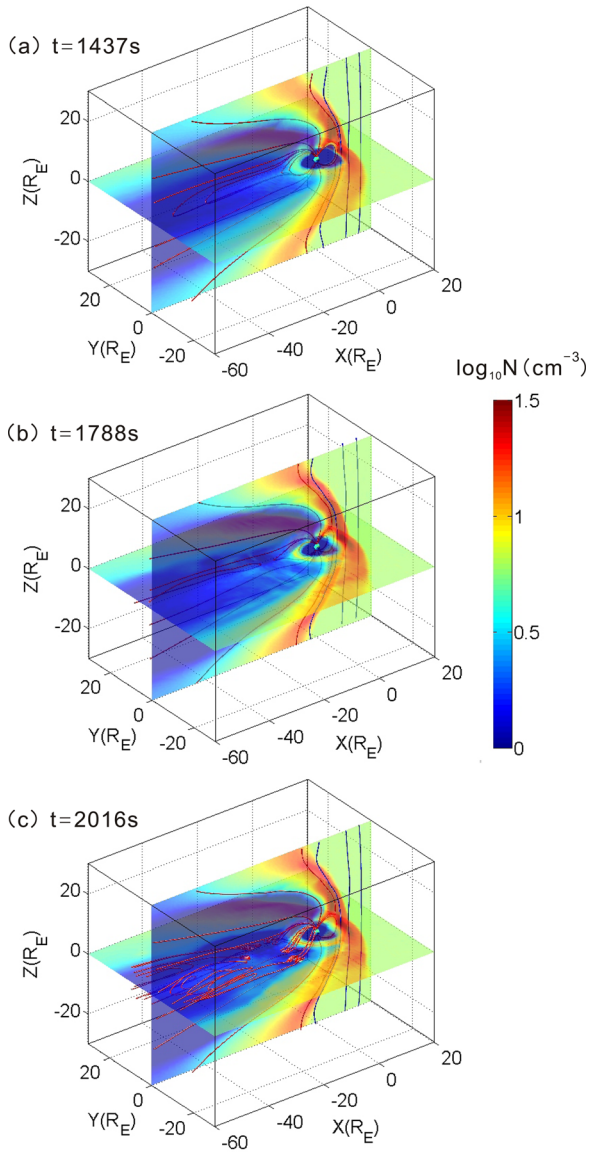


FIG. 1. Magnetic field lines in the 3-D perspective and contours of the ion density  $N$  in the  $z = 0$  (equatorial) and  $y = 0$  (noon-midnight meridian) planes at  $t =$  (a) 1437 s, (b) 1788 s, and (c) 2016 s.

$-15R_E$ , for  $y$  ranging from  $-10R_E$  to  $10R_E$ . These flux ropes have a spatial scale of several  $R_E$  ( $1R_E \sim 5R_E$ ) in both the GSM  $x$  and  $y$  directions, which is different from that in previous 3-D global-scale MHD simulations.<sup>21,26,27</sup> There is also a large-scale loop-type structure located in the mid-tail or even distant-tail region at  $x < -30R_E$ , which may be equivalent to the plasmoid predicted in the near-Earth neutral line (NENL) substorm model.<sup>14</sup> The ion density in the inner magnetosphere is further increased by continual particle injection from the magnetotail.

To present the structures of flux ropes and magnetotail reconnection more clearly, Fig. 2 depicts the 3-D magnetic field lines and contours of the ion flow velocity  $V_{ix}$  in the zoomed near-tail region of the equatorial ( $z = 0$ ) plane at  $t = 2016$  s. There are about six small-scale 3-D flux ropes (marked by “a,” “b,” “c,” “d,” “e,” and “f”) located in the near-tail region of the equatorial plane. The flux ropes “a,” “b,” and “c” are embedded in the tailward flow, and almost all the field lines of the

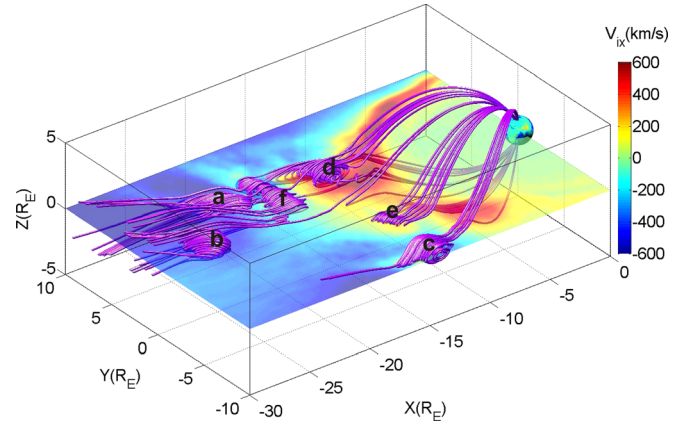


FIG. 2. Magnetic field lines and contour of the ion flow velocity  $V_{ix}$  in the zoomed near-tail region of the equatorial ( $z = 0$ ) plane at  $t = 2016$  s. Some of the flux ropes are marked by labels “a,” “b,” “c,” “d,” “e,” and “f.”

three flux ropes are connected to the large-scale plasmoid in the mid-tail. In contrast, the flux ropes “d” and “e” are embedded in the earthward high-speed flow (or BBF), and all the field lines of the two flux ropes are closed and connected to the Earth’s dipole field. The flux rope “f” is located in the vicinity of a reconnection site, and the structures of its field lines are more complicated. Some of the field lines are connected to the mid-tail large-scale plasmoid, and some are connected to the Earth’s dipole field. The remaining field lines are open, with one end connected to the Earth, and the other end to the tail.

Figures 3(a)–3(d) show, in turn, the structures of ion density  $N$ , ion flow velocity  $V_{ix}$ , and ion parallel and perpendicular temperatures  $T_{i||}$  and  $T_{i\perp}$  from  $x = -30R_E$  to  $-10R_E$  in the  $(x, z)$  plane along  $y = 4R_E$  at  $t = 2016$  s. There is a chain of three flux ropes in the near-tail region from  $x = -22R_E$  to  $x = -12R_E$ . The diameter of the flux ropes in our simulation is about  $2R_E$ , which is consistent with Geotail observations.<sup>17,43</sup> According to the ion flow velocity reversal, the primary X-line (with a higher reconnection rate) can be found around  $x = -18R_E$ . The flux rope “f” is generated within the vicinity of the primary X-line, and there are two more secondary X-lines (with lower reconnection rates) situated in the tailward and earthward flows of the primary X-line around  $x = -23R_E$  and  $x = -12R_E$ , respectively. Therefore, the two flux ropes “a” and “d” are generated between the primary X-line and secondary X-lines, and are then driven tailward and earthward, respectively. The ion density and temperatures (both parallel and perpendicular) peak around the center of the flux ropes, which is also shown in the top three panels in Fig. 3(e). Figure 3(e) shows the spatial variations of  $B_z$ ,  $N$ ,  $T_{i||}$ ,  $T_{i\perp}$ , and  $B$  along the path from point P1  $(-25, 4, 0.2)R_E$  to point P2  $(-10, 4, 0)R_E$ , which is marked by red line segments in the contours of Figs. 3(a)–3(d). The center of the flux ropes can be identified by the bipolar structure of  $B_z$ . The magnitude of the magnetic field exhibits a complicated pattern that has neither an in-phase nor anti-phase relationship with the ion density and temperatures. In all three flux ropes, “a,” “f,” and “d,” the magnitude of the magnetic field has a “crater-like” structure near the center of the flux ropes.

The magnetic and electric fields around the reconnection sites in the  $(x, z)$  plane along  $y = 4R_E$  at  $t = 2016$  s are

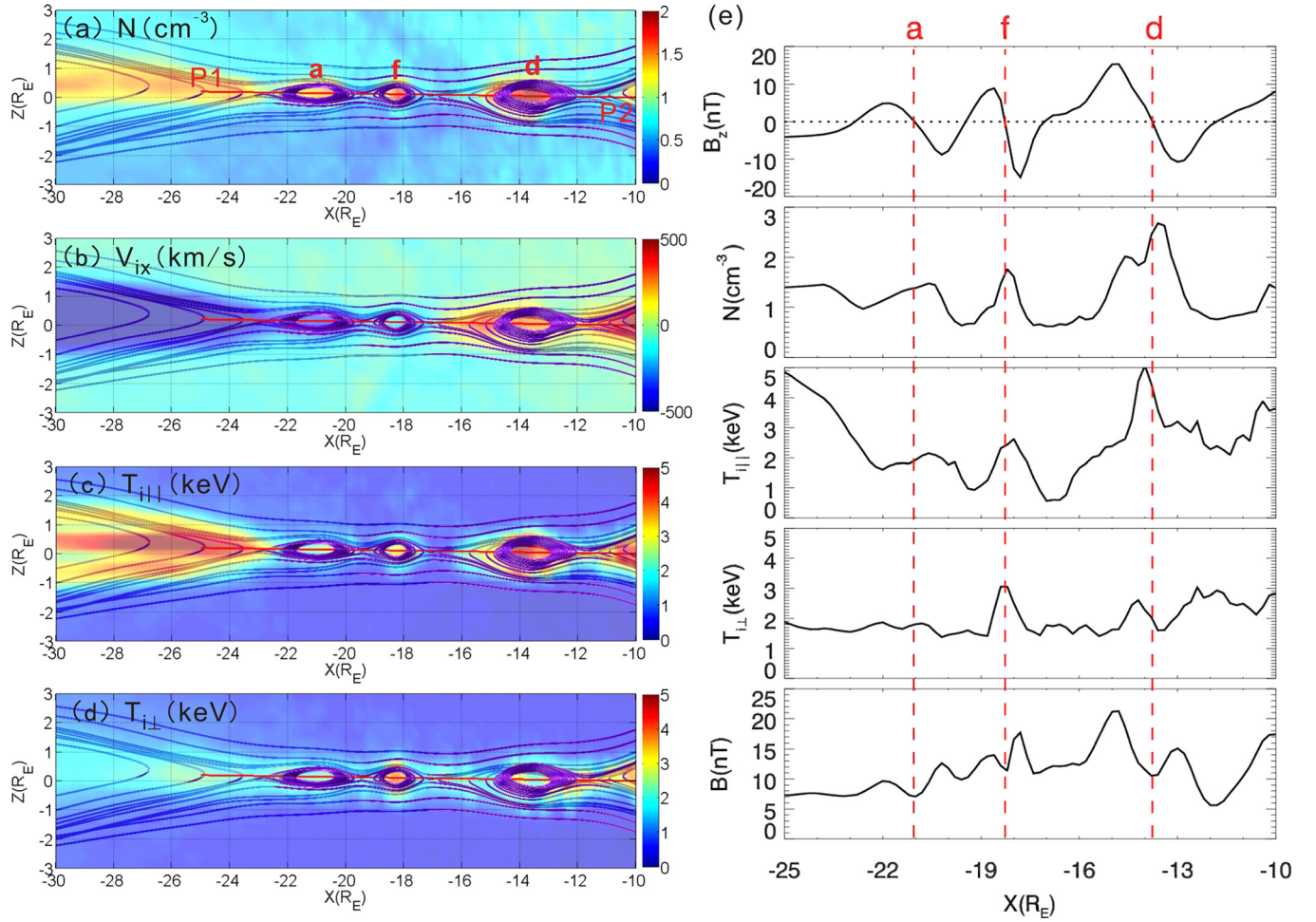


FIG. 3. Structure of (a) ion density  $N$ , (b) ion flow velocity  $V_{ix}$ , (c) ion parallel temperature  $T_{i||}$ , and (d) ion perpendicular temperature  $T_{i\perp}$  from  $x = -30R_E$  to  $-10R_E$  in the  $(x, z)$  plane along  $y = 4R_E$  at  $t = 2016$  s. (e) Spatial variations of  $B_z$ ,  $N$ ,  $T_{i||}$ ,  $T_{i\perp}$ , and  $B$  along the path from point P1 ( $-25R_E, 4R_E, 0.2R_E$ ) to point P2 ( $-10R_E, 4R_E, 0$ ). The flux ropes “a,” “d,” and “f” are the same flux ropes as shown in Fig. 2.

presented in detail in Fig. 4. The quadrupolar structure of  $B_y$  around the primary X-line at  $x = -18R_E$  (see Fig. 4(b)) clearly exhibits a signature of the Hall effect associated with collisionless fast reconnection. This ion inertial effect is self-consistently resolved in the hybrid model. The magnitude of the Hall magnetic field is about 10 nT, which is approximately 0.3 times the ambient magnetic field (35 nT). The Hall electric field  $E_x$  has a bipolar structure in the vicinity of each X-line (see Fig. 4(a)), and the Hall electric field  $E_z$  has a symmetric pattern and points to the center of the current sheet (see Fig. 4(e)). The direction of the Hall electric field  $\mathbf{E}_{Hall} = \mathbf{j} \times \mathbf{B}/N$  is basically perpendicular to the local magnetic field and pointing to the center of the flux rope, where  $\mathbf{j} \approx j_e \mathbf{e}_y$  is the cross-tail current. The quadrupolar structure of the out-of-plane Hall magnetic field and the corresponding bipolar structure of the in-plane Hall electric field are predicted in collisionless reconnection, and these structures have been reported in satellite observations.<sup>49–51</sup> Figure 4(c) presents  $E_y$ , which indicates the reconnection electric field or the convection electric field. Figure 4(d) shows the bipolar structures of  $B_z$ , corresponded to the series of flux ropes. Although the reconnection sites are spatially nonuniform and temporally unsteady (turbulent), the reconnection rate can be roughly given as  $R \approx V_{in}/V_A$ ,<sup>32</sup> where  $V_{in}$  is the inflow velocity. Figure 4(f) shows that the

reconnection ion inflow velocity  $V_{iz}$  is about 100 km/s  $\approx 1.1V_{A0}$ . The ion density in the vicinity of the reconnection site is about  $0.6\text{cm}^{-3} = 0.1N_0$ , and the magnitude of the ambient magnetic field is about  $35\text{ nT} = 3.5B_0$ . Therefore, the local Alfvén speed near the reconnection site is  $V_A \approx 11V_{A0}$ , and the ion inflow velocity is thus about  $0.1V_A$ , which gives a typical fast reconnection rate  $R \approx V_{in}/V_A \sim 0.1$ .

## B. Evolution of flux ropes

The time evolution of several typical tailward moving flux ropes is presented in Fig. 5, which shows the 3-D magnetic field lines and contours of the ion flow velocity  $V_{ix}$  in the equatorial plane at (a)  $t = 1859$  s, (b) 1923 s, (c) 1959 s, and (d) 2016 s. At  $t = 1859$  s, there is a primary reconnection X-line that is marked by “X” around  $x = -18R_E$ . A secondary X-line and a flux rope, marked by “g,” are embedded in the tailward outflow of the primary reconnection. The ion tailward flow speed is about  $V_{ix} = -500\text{ km/s}$ . The large-scale plasmoid in the mid-tail region of  $x < -30R_E$  is marked by “O.” The flux rope “g” is driven tailward quickly towards the O-type region (large-scale mid-tail plasmoid). At  $t = 1923$  s, the flux rope “g” merges into the large-scale mid-tail plasmoid. The reconnection diffusion region elongates

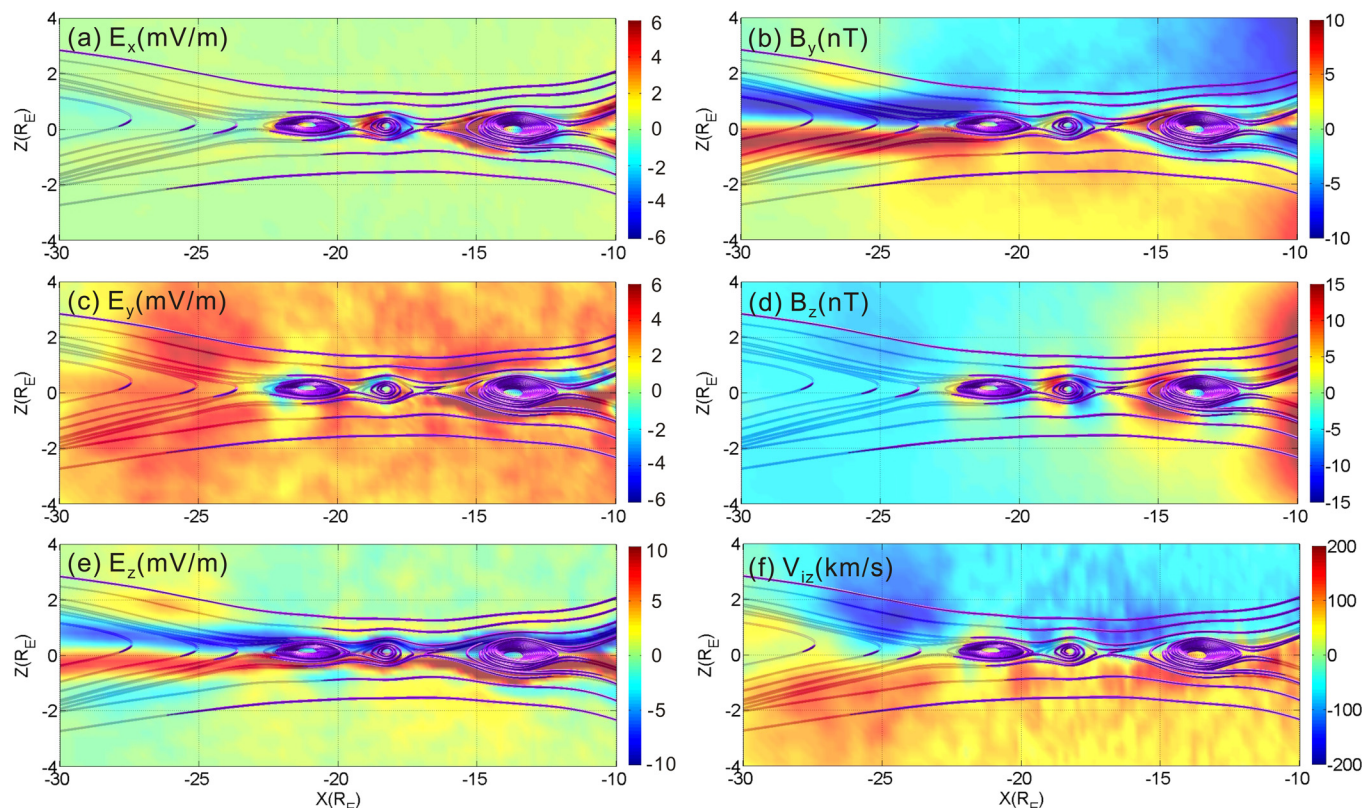


FIG. 4. Structure of the Hall magnetic and electric fields (a)  $E_x$ , (b)  $B_y$ , (c)  $E_y$ , (d)  $B_z$ , (e)  $E_z$ , and (f) ion inflow velocity  $V_{iz}$  from  $x = -30R_E$  to  $-10R_E$  in the  $(x, z)$  plane along  $y = 4R_E$  at  $t = 2016$  s.

as the reconnection process proceeds,<sup>52,53</sup> and two more flux ropes, marked by “h” and “i,” are generated almost simultaneously in the elongated reconnection diffusion region. The two flux ropes coalesce into each other and form a new flux rope

“h + i,” which is located at about  $x = -21R_E$  (see Fig. 5(c)). The new flux rope “h + i” is also driven tailward towards the large-scale plasmoid “O.” At  $t = 2016$  s, the flux rope “h + i” has moved to about  $x = -25R_E$ , which means that the flux rope

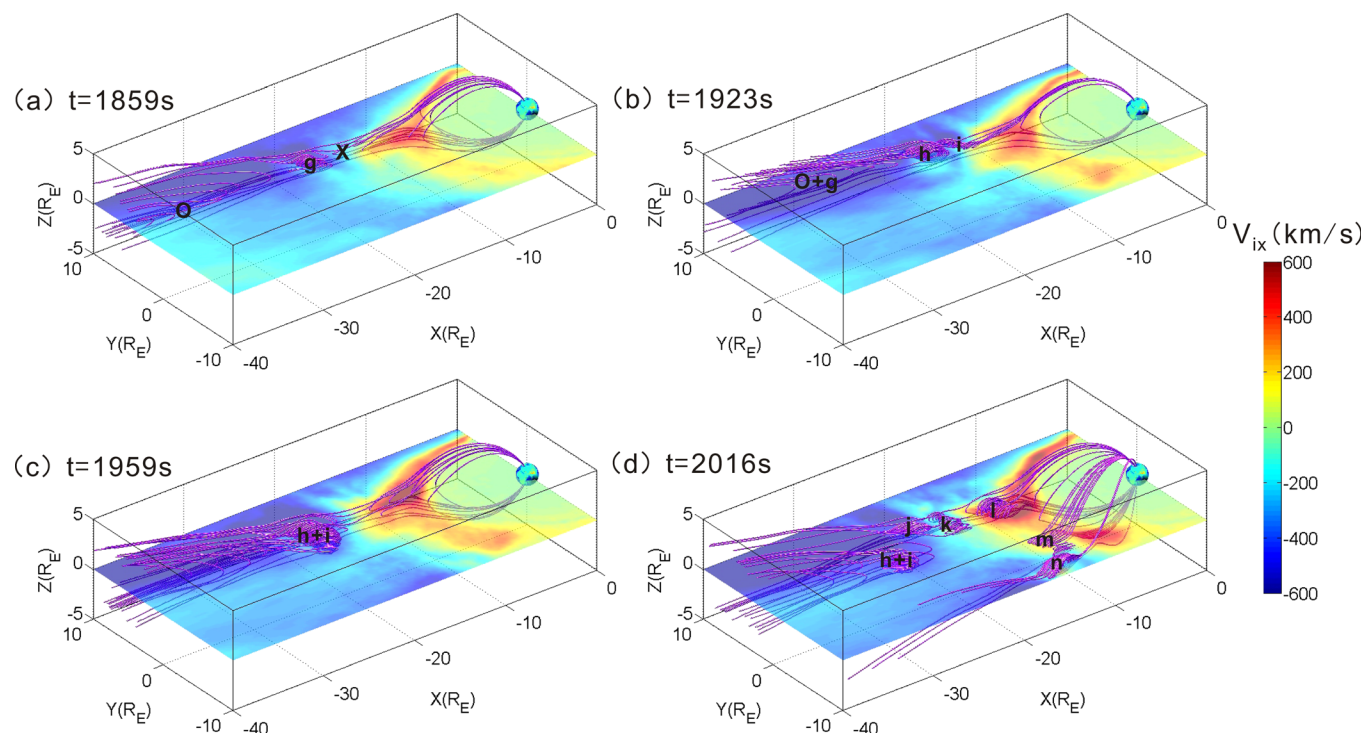


FIG. 5. Magnetic field lines and contours of the ion flow velocity  $V_{ix}$  in the equatorial plane at (a)  $t = 1859$  s, (b)  $1923$  s, (c)  $1959$  s, and (d)  $2016$  s. The labels “g,” “h,” “i,” “j,” “k,” “l,” “m,” and “n” denote some of the typical flux ropes during the evolution, and “O” denotes the mid- or distant-tail large-scale plasmoid.

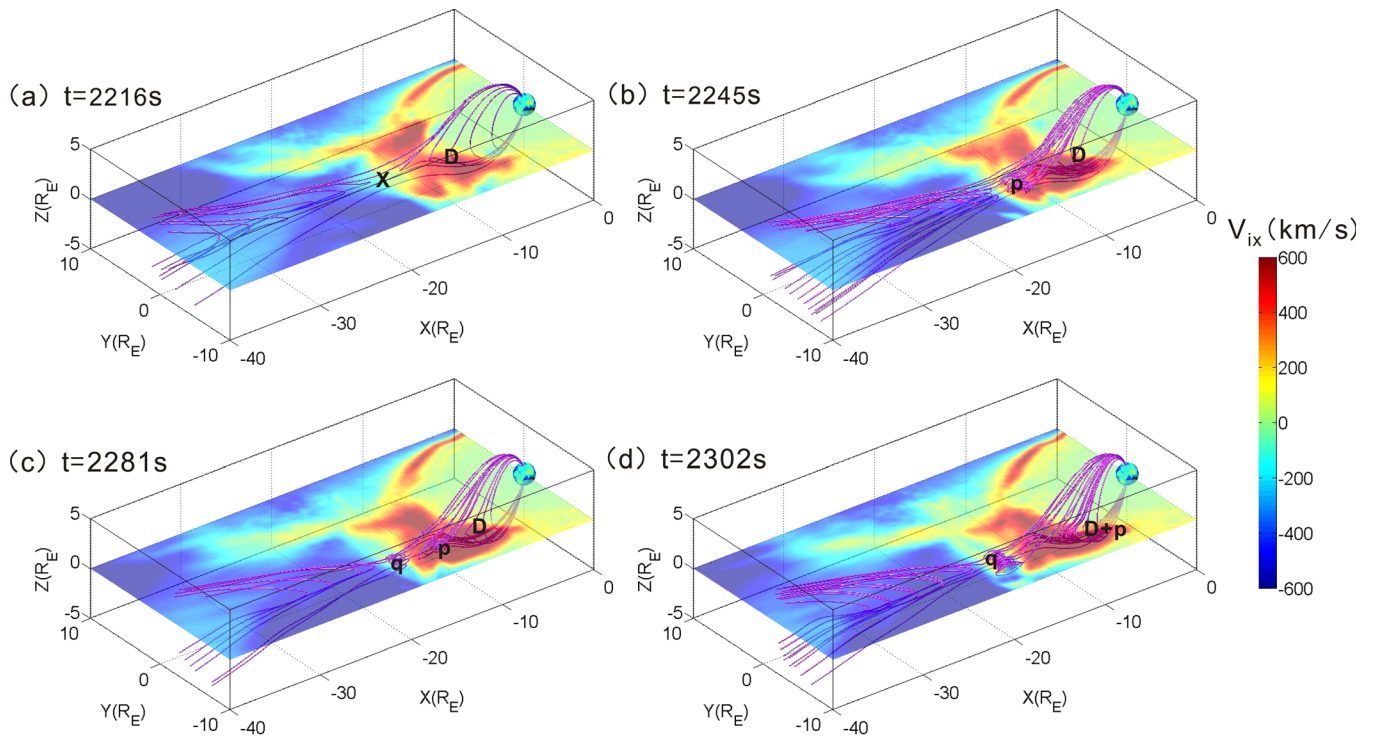


FIG. 6. Magnetic field lines and contours of the ion flow velocity  $V_{ix}$  in the equatorial plane at (a)  $t = 2216$  s, (b) 2245 s, (c) 2281 s, and (d) 2302 s. The labels “p” and “q” denote the flux ropes, and “D” denotes the near-Earth dipole-like region.

has moved  $4R_E$  during a period of 57 s. One can thus estimate the speed of tailward movement to be about 450 km/s. At the same time, five more flux ropes, marked by “j,” “k,” “l,” “m,” and “n,” are newly generated in the near-tail reconnection diffusion regions during this process (see Fig. 5(d)). In the magnetotail observations made by Slavin *et al.*,<sup>17</sup> this kind of tailward moving flux rope is termed a plasmoid-type flux rope.

Earthward moving BBF-type flux ropes are also observed in our 3-D global hybrid simulation. Figure 6 shows typical 3-D magnetic field lines and contours of the ion flow velocity  $V_{ix}$  in the equatorial plane at (a)  $t = 2216$  s, (b) 2245 s, (c) 2281 s, and (d) 2302 s. At  $t = 2216$  s, there is a near-tail reconnection at about  $x = -18R_E$ , which is marked by “X” in Fig. 6(a). The near-Earth region with a dipole-like magnetic field is denoted by “D.” As the reconnection diffusion region elongates, at  $t = 2245$  s, a flux rope, marked by “p,” is generated in the reconnection diffusion region at about  $x = -16.2R_E$ . The flux rope “p” is embedded in the earthward outflow (or BBF) of the near-tail reconnection and driven earthward. The maximum flow speed of the BBF is about 800 km/s. At  $t = 2281$  s, the flux rope “p” has moved to about  $x = -13.8R_E$ , or a distance of  $2.4R_E$ , during a period of 36 s, which gives a speed of motion of about 425 km/s. Meanwhile, a new flux rope, denoted by “q,” is generated at about  $x = -18R_E$ . At  $t = 2302$  s, the scale size of the flux rope “q” and the magnetic flux contained therein have both grown much larger. At the same time, the flux rope “p” has moved to about  $x = -10R_E$  and is about to merge into the near-Earth region with a dipole-like magnetic field. The plasma and magnetic flux in the flux rope “p” are then released and injected into the near-Earth region during the merging process. Note that in the magnetotail, the

multiple X-line reconnection (see Figs. 5 and 6) is spatially nonuniform and temporally unsteady, which leads to a turbulent reconnection layer in the near-tail.

Figure 7 demonstrates that a flux rope can be strongly tilted in the GSM  $(x, y)$  plane during its evolution and

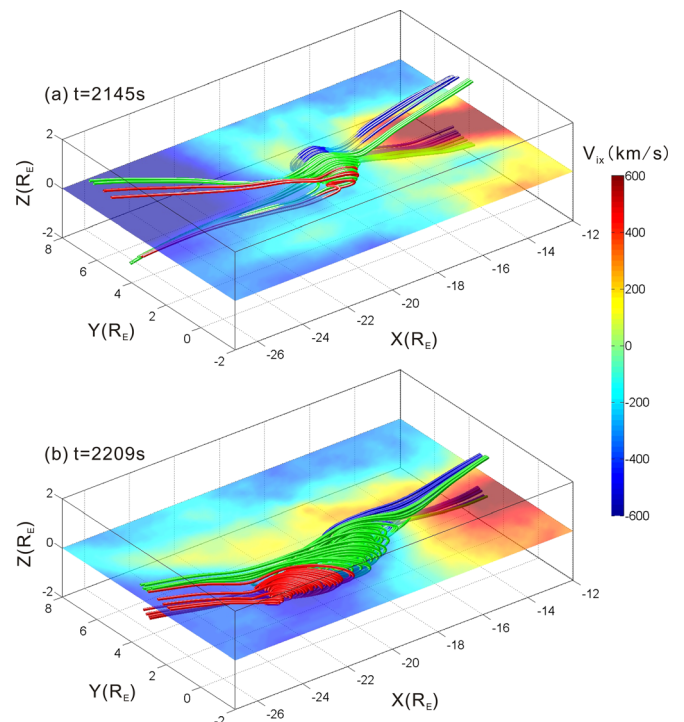


FIG. 7. Typical magnetic field lines and contours of the ion flow velocity  $V_{ix}$  in the equatorial plane at (a)  $t = 2145$  s and (b) 2209 s. Blue field lines have an Earth-to-Earth (closed) topology, the green field lines an Earth-to-tail (semi-open) topology, and the red field lines a tail-to-tail (open) topology.

propagation. At  $t = 2145$  s, a newly generated flux rope is located at  $x \approx -18R_E$  and extends from  $y = 2R_E$  to  $4R_E$ . At  $t = 2009$  s, the flux rope is strongly tilted at an angle of about  $65^\circ$ . During the time interval of 64 s, the diameter of the flux rope has increased. According to the reversal of the ion flow  $V_{ix}$ , the duskside end of the flux rope (at  $x \approx -17R_E$ ,  $y \approx 3R_E$ ) is embedded in the earthward flow of a primary reconnection X-line. In contrast, the dawnside end of the flux rope (at  $x \approx -23R_E$ ,  $y \approx 0.5R_E$ ) is embedded in the tailward flow of another primary X-line. The tilt of the flux rope can be explained by the nonuniform and unsteady (or turbulent) multiple X-line reconnection; i.e., on the duskside (dawnside) of the flux rope, the primary X-line is on the tailward (earthward) side of the flux rope, and the duskside (dawnside) of the flux rope is thus driven earthward (tailward) by the reconnection high-speed outflow. As the imbalance of the reconnection rates between the primary and secondary X-lines continues to grow, the flux rope tilts more. Topologies of the magnetic field lines can also be used to explain the tilt of the flux rope. In Fig. 7, the blue field lines have an Earth-to-Earth (closed) topology, the green field lines an Earth-to-tail (semi-open) topology, and the red field lines a tail-to-tail (open) topology. The magnetic tension forces of the blue (red) field lines drive the flux rope earthward (tailward). As the reconnection on the duskside (dawnside) of the flux rope proceeds, at the primary X-line, more green field lines are reconnected with the semi-open field lines (coming from the lobe region) and change into blue (red) field lines, which pulls the duskside (dawnside) of the flux rope earthward (tailward). Such opposing magnetic tension forces acting on the two ends tilt the flux rope.

During the coalescence and merging of the flux ropes, the ions are heated in the magnetotail plasma sheet and the near-Earth dipole-like region. Figure 8 presents the detailed time evolution of the coalescence between two flux ropes (“h” and “i” marked in Fig. 5(b)). Zoomed-in contours of the

parallel (left column) and perpendicular (right column) temperatures are shown in this figure from  $x = -30R_E$  to  $-10R_E$  in the  $(x, z)$  plane along  $y = 4R_E$ , in a uniformly spaced time sequence of  $t = 1923$ , 1930, 1938, and 1945 s. At  $t = 1923$  s, there are two small flux ropes at about  $x = -19R_E$  and  $x = -16R_E$ , and their maximum ion parallel temperature is about 2.5 keV. The two flux ropes gradually merge into each other. At  $t = 1945$  s, the two flux ropes finally coalesce into a new flux rope, and the maximum ion parallel temperature of the new flux rope is about 4.5 keV. The ion parallel temperature inside the flux ropes is significantly increased after the coalescence of the flux ropes. In contrast, there is no obvious ion perpendicular temperature increase during the coalescence of the flux ropes.

The ion heating and/or acceleration on a longer time scale is shown in Fig. 9, which depicts the ion flow velocity  $V_{ix}$  and ion parallel and perpendicular temperatures  $T_{i\parallel}$  and  $T_{i\perp}$  from  $x = -40R_E$  to  $x = 0$  in the noon-midnight meridian ( $y = 0$ ) plane at (a)  $t = 2000$  s and (b) 2500 s. At  $t = 2000$  s, there is a primary reconnection proceeding around  $x = -18R_E$ . In the tailward outflow of the primary reconnection X-line, there is a secondary reconnection X-line as well as a resulting flux rope. The maximum temperature is about 2.5 keV. At  $t = 2500$  s, the primary reconnection X-line is located at about  $x = -27R_E$ , and two flux ropes are driven earthward by the reconnection earthward high-speed outflow. During the period of 500 s, numerous flux ropes are generated in the near-tail plasma sheet (not shown). These flux ropes are then driven earthward or tailward by the reconnection high-speed outflows. Eventually, the earthward propagating flux ropes merge into the near-Earth dipole-like region, and the tailward propagating flux ropes merge into the mid-tail large-scale plasmoid. Therefore, the near-tail plasma sheet and near-Earth dipole-like regions are significantly heated. The maximum temperature is about 5.5 keV. The ion temperature anisotropy can be easily observed. The

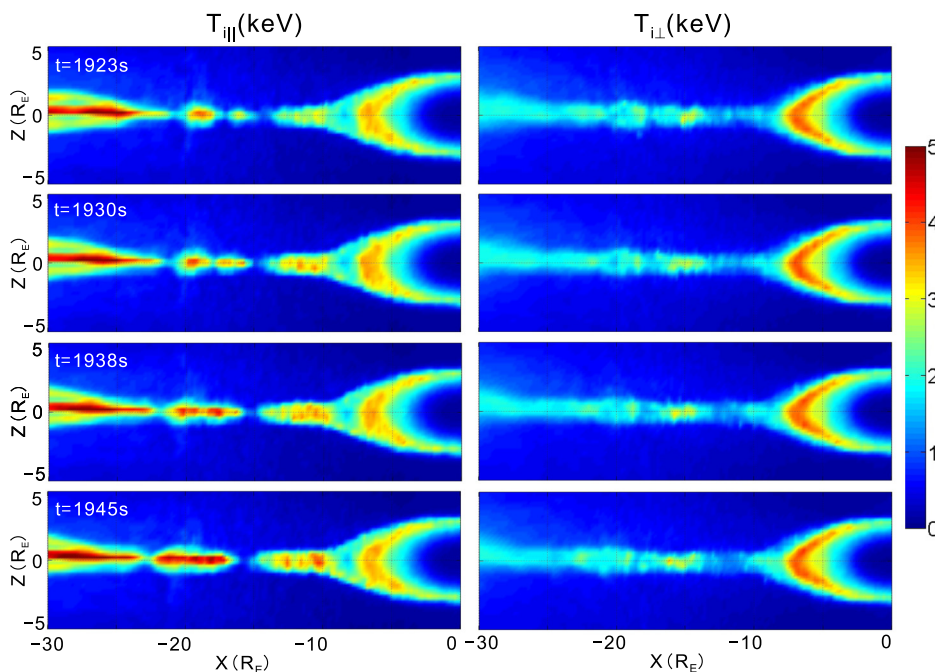


FIG. 8. Contours of the parallel (left column) and perpendicular (right column) temperatures  $T_{i\parallel}$  and  $T_{i\perp}$  from  $x = -30R_E$  to  $x = 0$  in the  $(x, z)$  plane along  $y = 5R_E$ , in a uniformly-spaced time sequence of  $t = 1923$ , 1930, 1938, and 1945 s.

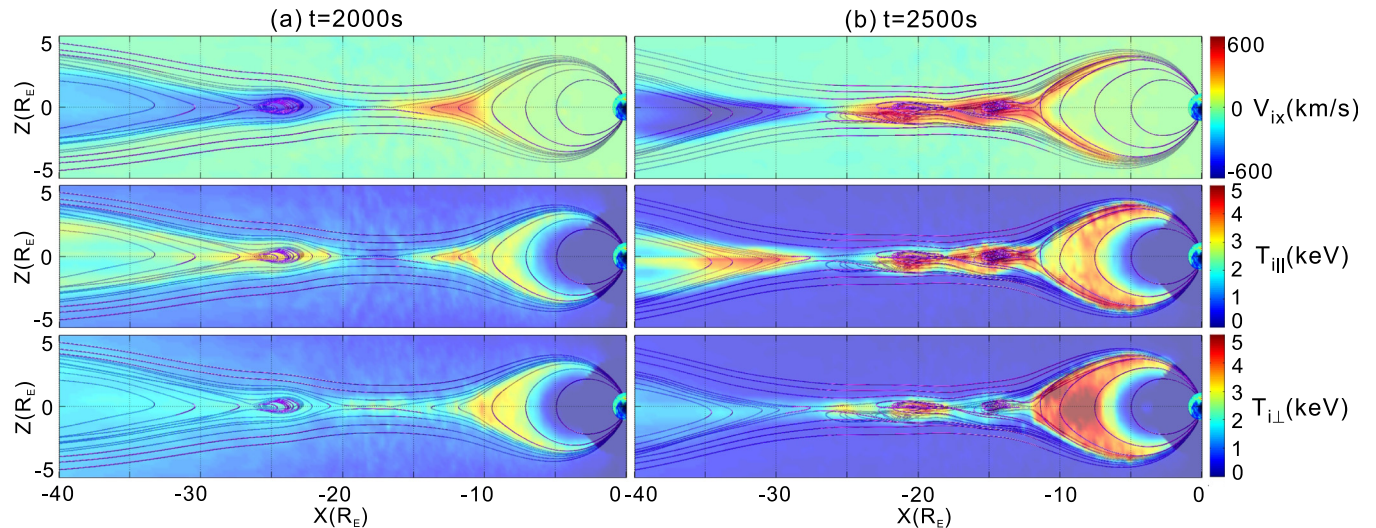


FIG. 9. Contours of the ion flow velocity  $V_{ix}$ , ion parallel and perpendicular temperatures  $T_{||}$ ,  $T_{\perp}$  from  $x = -40R_E$  to  $x = 0$  in the noon-midnight meridian ( $y = 0$ ) plane at (a)  $t = 2000$  s and (b) 2500 s.

ion parallel temperature is higher than the ion perpendicular temperature in the reconnection high-speed outflows while the ion perpendicular temperature is higher than the ion parallel temperature in the near-Earth dipole-like region.

### C. Ion velocity distributions and energy spectra

The ion velocity distributions in the magnetotail reconnection and the near-Earth dipole-like regions are shown in Fig. 10. Plotted in Fig. 10 are the distributions  $f(v_{px}, v_{py})$  (top panels) and  $f(v_{px}, v_{pz})$  (bottom panels) at  $t = 2495$  s, at six different locations: (a)  $(x, y, z) = (-25, 0, 0)R_E$  in the vicinity of the primary X-line, (b)  $(-31, -3, 0)R_E$  on the tailward side of the primary X-line, (c)  $(-16, 0, 0)R_E$  in an earthward moving flux rope, (d)  $(-22, 0, 0)R_E$  inside another earthward moving flux rope, (e)  $(-4.7, 6.5, 0)R_E$  on the duskside flank of the near-Earth dipole-like region, and (f)

$(0, -8, 0)R_E$  on the dawnside flank of the near-Earth dipole-like region. At the time  $t = 2495$  s, the primary X-line has been retreated to  $x \approx -25R_E$ . In the vicinity of the primary X-line (see Fig. 10(a)), the ions are relatively cold and the temperature is anisotropic, with  $T_x < T_y \approx T_z$ . The velocity distribution is shifted downward and centered at about  $v_{py} \approx -250$  km/s. The shift is caused by the  $\mathbf{E} \times \mathbf{B}$  drift associated with the Hall electric field.<sup>44</sup> On the tailward side of the primary X-line (see Fig. 10(b)), one can observe a high-speed tailward ion beam, centered at about  $v_{px} = -900$  km/s, coexisting with another lower-speed ion beam that is also moving tailward owing to the multiple X-line reconnection. In the earthward propagating flux rope at  $x = -16R_E$  (see Fig. 10(c)), there is a relatively weak accelerated earthward ion beam with a peak velocity of about  $v_{px} \approx 250$  km/s. This ion population coexists with a colder inflow (to the X-line) of ions with the velocity in the  $x$

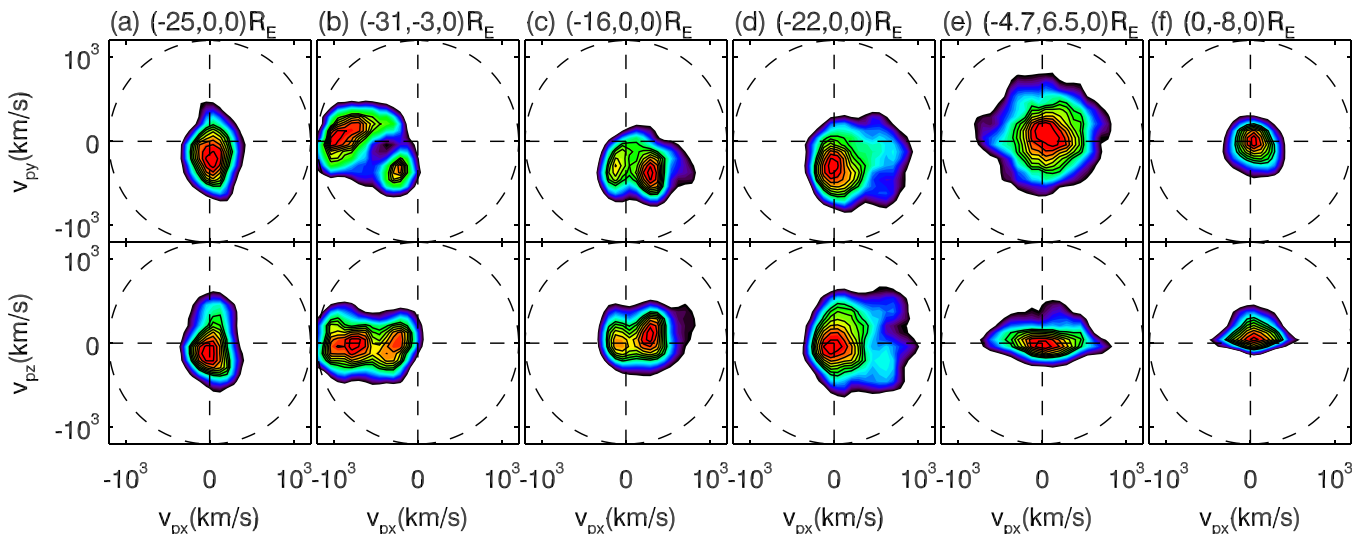


FIG. 10. Ion velocity distributions  $f(v_{px}, v_{py})$  (top panels) and  $f(v_{px}, v_{pz})$  (bottom panels) at  $t = 2495$  s, at six different locations: (a)  $(x, y, z) = (-25, 0, 0)R_E$  in the vicinity of the primary X-line, (b)  $(-31, -3, 0)R_E$  on the tailward side of the primary X-line, (c)  $(-16, 0, 0)R_E$  in an earthward moving flux rope, (d)  $(-22, 0, 0)R_E$  inside another earthward moving flux rope, (e)  $(-4.7, 6.5, 0)R_E$  on duskside flank of the near-Earth dipole-like region, and (f)  $(0, -8, 0)R_E$  on dawnside flank of the near-Earth dipole-like region.

direction  $v_{px} \approx -100$  km/s. There is a similar downward drift in the inflow and outflow beams. At  $x = -22R_E$  inside another earthward moving flux rope (see Fig. 10(d)), the ion temperature is higher than that in the vicinity of the X-line, which indicates that there is a heating process during the formation and evolution of the flux rope. Note that the ions are also heated in the flux rope at  $x = -16R_E$ . Eventually, the earthward propagating flux ropes and high-speed flows will interact with the near-Earth dipole-like region, directly affecting the plasma environment in this region. Figures 10(e) and 10(f) present the ion velocity distributions in the near-Earth dipole-like region. On both the duskside and dawnside flanks of the region, the ion heating is mainly in the direction perpendicular to the magnetic field (i.e., nearly in the  $z$  direction) at these equatorial locations. In the plane perpendicular to the magnetic field, the ion distribution is nearly gyrotropic. Note that on the dawnside flank of the region, the ions are colder and less energetic. This is because the higher energy ions drift westward (duskward) owing to the magnetic gradient and curvature drift.

To further demonstrate the ion acceleration and heating processes associated with the flux ropes and reconnection in the magnetotail, Fig. 11 plots normalized ion energy spectra at  $t = 2495$  s, at the three different locations shown in Figs. 10(a)–10(c). At  $x = -25R_E$  (black curve) in the vicinity of the primary X-line, the spectrum exhibits two parts of the different particle distribution, one at lower energy and one at higher energy. The accelerated high energy part begins from about 12 keV, peaks at about 15 keV, and extends beyond 20 keV. The ion temperature, however, is low, which suggests that in the vicinity of the primary X-line, the ion energization process is dominated by acceleration instead of heating. The ion temperature is enhanced at  $x = -31R_E$  (in the tailward outflow, red curve) and  $x = -16R_E$  (inside an earthward propagating flux rope, green curve). The heating may be due to the existence of the reconnection electric field or wave-particle interaction associated with Alfvén and compressional waves.<sup>44,54–57</sup> Parallel mixing of ion beams along

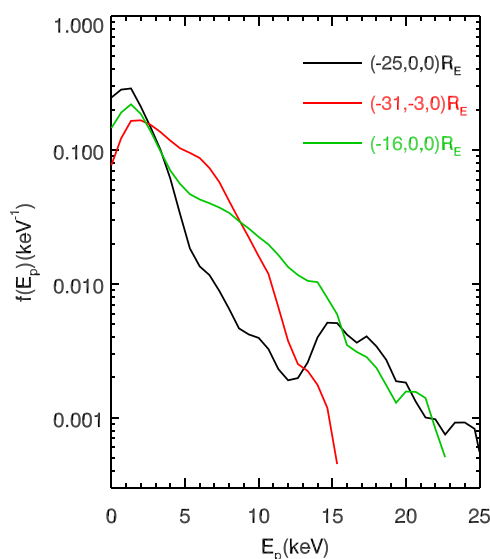


FIG. 11. Normalized ion energy spectra at  $t = 2495$  s, at three different locations shown in Figs. 10(a)–10(c).

field lines may also play an important role in the parallel heating during multiple X-line reconnection.<sup>19,58</sup> It should also be noted that at  $x = -16R_E$  (green curve) inside the earthward propagating flux rope, the ions are not only heated but also accelerated to high energy of about 25 keV.

#### IV. CONCLUSIONS AND DISCUSSION

In this paper, the generations of fast reconnection at multiple X-lines and a number of small-scale (several  $R_E$  in the  $x$  and  $y$  directions), 3-D flux ropes were simulated for the first time with a 3-D hybrid simulation model for a global-scale configuration of the magnetosphere. Although previous 3-D MHD simulations have been performed to investigate the large-scale plasmoid,<sup>33–39</sup> the structure and evolution of the plasmoid in the MHD simulations is relatively simple in the absence of kinetic effects. In our 3-D global hybrid simulation, small-scale 3-D flux ropes undergoing various kinds of evolution (earthward/tailward propagations, tilt in the equatorial plane, merging and coalescing) were observed. The main conclusions are as follows:

- (1) Under the southward IMF, there is magnetic reconnection with multiple X-lines in the near-tail at  $x = -30R_E \sim -15R_E$ . The magnetotail reconnection layer is turbulent with a nonuniform structure and unsteady evolution, and exhibits properties of collisionless reconnection with the Hall effect. The reconnection rate can be roughly given as  $R \approx V_{in}/V_A$ ,<sup>32</sup> where  $V_{in}$  is the inflow velocity. The typical reconnection rate in our simulation is  $\sim 0.1$ , which is in the scope of fast reconnection.
- (2) A number of small-scale 3-D flux ropes are continually generated through multiple X-line reconnection in the near-tail, and they then propagate earthward or tailward. Eventually, these earthward or tailward propagating flux ropes merge into the near-Earth region or the mid-/distant-tail plasmoid, respectively. The ion density and temperatures (parallel and perpendicular) peak at the center of the flux ropes, while the magnitude of the magnetic field has a crater-like structure near the center of the flux ropes.
- (3) A flux rope can be strongly tilt in the  $(x, y)$  plane during its evolution and propagation. The tilt is caused by the turbulent, nonuniform, and unsteady multiple X-line reconnection, or more specifically, by the opposing magnetic tension forces acting on the duskside and dawnside ends of the flux rope.
- (4) Coalescence of the flux ropes is observed during the evolution of the flux ropes. The ion parallel temperature in the newly generated flux rope(s) is enhanced during the coalescence, while the ion perpendicular temperature does not change greatly.
- (5) The ion velocity distributions and energy spectra show that the ions are accelerated in the vicinity of the reconnection X-lines, and heated in the flux ropes and reconnection high-speed outflows.

In our simulation, the reconnection rate of the magnetotail reconnection is  $\sim 0.1$ , which is consistent with the GEM reconnection challenge.<sup>59</sup> In the fully kinetic (or full particle)

model, the tiny-scale (on the order of several electron inertial lengths) electron diffusion region of reconnection cannot be resolved, and the reconnection electric field in the electron diffusion region is mainly contributed by the off-diagonal electron pressure tensor term.<sup>60,61</sup> However, in the 3-D global hybrid model, the electron diffusion region is too small to resolve, and the electron kinetic effects are not considered. According to the generalized Ohm's law (Eq. (3)), in our 3-D hybrid model, the reconnection electric field in the vicinity of the reconnection point (or electron diffusion region) is contributed by the collision term and the diagonal electron pressure term  $-(1/N)\partial p_e/\partial y$ . Therefore, in our simulations, the reconnection rate cannot be represented by the reconnection electric field at the reconnection point. Instead, we use the inflow velocity to represent the reconnection rate.<sup>32</sup>

In 3-D MHD simulations, the scale length of the generated magnetotail flux ropes in the radial direction is very large, on the order of several tens of  $R_E$ .<sup>33–39</sup> Such large-scale flux ropes, however, are more likely to be equivalent to the mid- or distant-tail large-scale plasmoid predicted in the NENL substorm model.<sup>14</sup> In contrast, the flux ropes obtained in our 3-D global hybrid simulation are located in the near-tail region, and the diameter of the flux ropes is on the order of several  $R_E$ , which is consistent with Geotail observations.<sup>17,43</sup> In our hybrid simulation, the spatial scale of the flux ropes in the dawn-dusk direction is also very small (on the order of several  $R_E$ ) and does not extend across the entire cross section of the magnetotail, which is contrary to previous models and MHD simulation results.<sup>34,35,38</sup> Similarly, ARTEMIS observations near lunar orbit suggest that the flux ropes are spatially confined in the dawn-dusk direction.<sup>62</sup>

Tilted flux ropes have been observed by ARTEMIS in the Earth's magnetotail.<sup>63</sup> In our simulation, tilted flux ropes were formed by the magnetotail multiple X-line reconnection, which is spatially nonuniform and temporally unsteady. For the tilted flux rope, the simulation results show that, on the duskside (dawnside) of the flux rope, the imbalance of the reconnection rates at the primary and secondary X-lines leads to the earthward (tailward) movement of the flux rope. This kind of opposite movements at the two ends of the flux rope results in the tilt of the flux rope. Furthermore, our simulation gives a clear picture of the entire evolution process of the flux ropes in the magnetotail, from their formation to eventual dissipation. All tailward moving flux ropes containing accelerated/heated plasmas eventually merge into the mid- or distant-tail large-scale plasmoid, which contributes to the return of the energy, mass, and magnetic flux to the interplanetary space. Such loss ensures the balance of the global magnetospheric convection during substorms. All earthward moving flux ropes eventually merge into the near-Earth dipole-like region. The accelerated/heated ions are thus injected into the near-Earth region, which contributes to particle injection from the magnetotail to the inner magnetosphere. During this process, magnetic flux and energy are also transported into the dipole-like region, which leads to near-Earth magnetic dipolarization associated with substorms.<sup>64,65</sup>

## ACKNOWLEDGMENTS

This work was supported by 973 Program (Nos. 2012CB825602 and 2013CBA01503), the National Science Foundation of China, Grant Nos. 41331067, 11235009, 41274124, 41274144, and 41121003, CAS Key Research Program KZZD-EW-01-4, and NSF Grant PH-0903794 to Auburn University. Computer resources were provided by the National Supercomputer Center of China in Tianjin, and the Alabama Supercomputer Center. The authors also thank D. W. Swift for his help and discussions on the code development. The results in this paper are generated from our computer simulation code as described in Sec. II. The data can be obtained by emailing the corresponding author.

- <sup>1</sup>W. J. Hughes and D. G. Sibeck, *Geophys. Res. Lett.* **14**(6), 636–639 (1987), doi:10.1029/GL014i006p00636 (1987).
- <sup>2</sup>J. Birn, M. Hesse, and K. Schindler, *J. Geophys. Res.* **94**(A1), 241–251, doi:10.1029/JA094iA01p00241 (1989).
- <sup>3</sup>M. B. Moldwin and W. J. Hughes, *J. Geophys. Res.* **96**(A8), 14051–14064, doi:10.1029/91JA01167 (1991).
- <sup>4</sup>J. A. Slavin, C. J. Owen, and M. M. Kuznetsova, *Geophys. Res. Lett.* **22**(15), 2061–2064, doi:10.1029/95GL01977 (1995).
- <sup>5</sup>R. P. Lepping, D. H. Fairfield, J. Jones, L. A. Frank, W. R. Paterson, S. Kokubun, and T. Yamamoto, *Geophys. Res. Lett.* **22**(10), 1193–1196, doi:10.1029/94GL01114 (1995).
- <sup>6</sup>R. P. Lepping, J. A. Slavin, M. Hesse, J. A. Jones, and A. Szabo, *J. Geomagn. Geoelectr.* **48**(5–6), 589–601, doi: (1996).
- <sup>7</sup>D. N. Baker, T. I. Pulkkinen, V. Angelopoulos, W. Baumjohann, and R. L. McPherron, *J. Geophys. Res.* **101**(A6), 12975–13010, doi:10.1029/95JA03753 (1996).
- <sup>8</sup>J. F. Drake, M. Swisdak, H. Che, and M. A. Shay, *Nature* **443**, 553–556 (2006).
- <sup>9</sup>X. R. Fu, Q. M. Lu, and S. Wang, *Phys. Plasmas* **13**, 012309 (2006).
- <sup>10</sup>P. L. Pritchett, *J. Geophys. Res.* **111**, A10212, doi:10.1029/2006JA011793 (2006).
- <sup>11</sup>L. J. Chen, A. Bhattacharjee, P. A. Puhl-Quinn, H. Yang, N. Bessho, S. Imada, S. Mühlbachler, P. W. Daly, B. Lefebvre, Y. Khotyaintsev, A. Vaivads, F. Fazakerley, and E. Georgescu, *Nat. Phys.* **4**, 19–23 (2008).
- <sup>12</sup>R. S. Wang, Q. M. Lu, A. M. Du, and S. Wang, *Phys. Rev. Lett.* **104**(17), 175003 (2010).
- <sup>13</sup>M. Oka, M. Fujimoto, I. Shinohara, and T. D. Phan, *J. Geophys. Res.* **115**, A08223, doi:10.1029/2010JA015392 (2010).
- <sup>14</sup>E. W. Hones, *J. Geophys. Res.* **82**(35), 5633–5640, doi:10.1029/JA082i035p05633 (1977).
- <sup>15</sup>M. B. Moldwin and W. J. Hughes, *J. Geophys. Res.* **97**, 19259, doi:10.1029/92JA01598 (1992).
- <sup>16</sup>M. B. Moldwin and W. J. Hughes, *J. Geophys. Res.* **99**(A1), 183–198, doi:10.1029/93JA02102 (1994).
- <sup>17</sup>J. A. Slavin, R. P. Lepping, J. Gjerloev, D. H. Fairfield, M. Hesse, C. J. Owen, M. B. Moldwin, T. Nagai, A. Ieda, and T. Mukai, *J. Geophys. Res.* **108**(A1), 1015, doi:10.1029/2002JA009557 (2003).
- <sup>18</sup>Q. G. Zong, T. A. Fritz, Z. Y. Pu, S. Y. Fu, D. N. Baker, H. Zhang, A. T. Lui, I. Vogiatzis, K. H. Glassmeier, A. Korth, P. W. Daly, A. Balogh, and H. Reme, *Geophys. Res. Lett.* **31**(18), L18803, doi:10.1029/2004GL020692 (2004).
- <sup>19</sup>J. P. Eastwood, D. G. Sibeck, J. A. Slavin, M. L. Goldstein, B. Lavraud, M. Sitnov, S. Imber, A. Balogh, E. A. Lucek, and I. Dandouras, *Geophys. Res. Lett.* **32**(11), L11105, doi:10.1029/2005GL022509 (2005).
- <sup>20</sup>S. M. Imber, J. A. Slavin, H. U. Auster, and V. Angelopoulos, *J. Geophys. Res.* **116**, A02201 (2011).
- <sup>21</sup>K. Schindler, *J. Geophys. Res.* **79**, 2803, doi:10.1029/JA079i019p02803 (1974).
- <sup>22</sup>L. C. Lee and Z. F. Fu, *Geophys. Res. Lett.* **12**(2), 105–108, doi:10.1029/GL012i002p00105 (1985).
- <sup>23</sup>M. Hesse, K. Schindler, J. Birn, and M. Kuznetsova, *Phys. Plasmas* **6**(5), 1781–1795 (1999).
- <sup>24</sup>D. Krauss-Varban and N. Omidi, *Geophys. Res. Lett.* **22**, 3271, doi:10.1029/95GL03414 (1995).
- <sup>25</sup>Y. Lin and D. W. Swift, *J. Geophys. Res.* **101**(A9), 19859–19870, doi:10.1029/96JA01457 (1996).

- <sup>26</sup>R. F. Lottermoser, M. Scholer, and A. P. Matthews, *J. Geophys. Res.* **103**(A3), 4547–4559, doi:10.1029/97JA01872 (1998).
- <sup>27</sup>H. Karimabadi, D. Krauss-Varban, N. Omid, and H. X. Vu, *J. Geophys. Res.* **104**(A6), 12313–12326, doi:10.1029/1999JA900089 (1999).
- <sup>28</sup>C. Huang, Q. Lu, H. Zhang, M. Wu, Q. Dong, S. Lu, and S. Wang, *Phys. Plasmas* **19**, 042111 (2012).
- <sup>29</sup>C. Huang, Q. Lu, S. Lu, P. Wang, and S. Wang, *J. Geophys. Res.* **119**, 798–807, doi:10.1002/2013JA019249 (2014).
- <sup>30</sup>Y. Lin and D. W. Swift, *J. Geophys. Res.* **107**(A11), 1373, doi:10.1029/2002JA009308 (2002).
- <sup>31</sup>W. Daughton, V. Roytershteyn, H. Karimabadi, L. Yin, B. J. Albright, B. Bergen, and K. J. Bowers, *Nat. Phys.* **7**, 539–542 (2011).
- <sup>32</sup>W. Daughton, T. K. M. Nakamura, H. Karimabadi, V. Roytershteyn, and B. Loring, *Phys. Plasmas* **21**, 052307 (2014).
- <sup>33</sup>A. Usadi, A. Kageyama, K. Watanabe, and T. Sato, *J. Geophys. Res.* **98**(A5), 7503–7517, doi:10.1029/92JA02078 (1993).
- <sup>34</sup>R. J. Walker, T. Ogino, J. Raeder, and M. Ashour-Abdalla, *J. Geophys. Res.* **98**(A10), 17235–17249, doi:10.1029/93JA01321 (1993).
- <sup>35</sup>T. Ogino, R. J. Walker, and M. Ashour-Abdalla, *J. Geophys. Res.* **99**(A6), 11027–11042, doi:10.1029/93JA03313 (1994).
- <sup>36</sup>J. Raeder, R. J. Walker, and M. Ashour-Abdalla, “The structure of the distant geomagnetic tail during long periods of northward IMF,” *Geophys. Res. Lett.* **22**(4), 349–352, doi:10.1029/94GL03380 (1995).
- <sup>37</sup>J. Raeder, in *Substorms 2* (Geophys. Inst., Univ. of Alaska, Fairbanks 1994), p. 561.
- <sup>38</sup>N. L. Farr, D. N. Baker, and M. Wiltberger, *J. Geophys. Res.* **113**(A12), A12202, doi:10.1029/2008JA013328 (2008).
- <sup>39</sup>M. El-Alaoui, M. Ashour-Abdalla, R. J. Walker, V. Peromian, R. L. Richard, V. Angelopoulos, and A. Runov, *J. Geophys. Res.* **114**, A08221, doi:10.1029/2009JA014133 (2009).
- <sup>40</sup>R. M. Winglee, E. Harnett, and A. Kidder, *J. Geophys. Res.* **114**, A09213, doi:10.1029/2008JA013750 (2009).
- <sup>41</sup>R. M. Winglee, *J. Geophys. Res.* **109**, A09206, doi:10.1029/2004JA010385 (2004).
- <sup>42</sup>E. W. Hones, *Geophys. Res. Lett.* **11**, 5, doi:10.1029/GL011i001p00005 (1984).
- <sup>43</sup>J. A. Slavin, R. P. Lepping, J. Gjerloev, M. L. Goldstein, D. H. Fairfield, M. H. Acuna, A. Balogh, M. Dunlop, M. G. Kivelson, K. Khurana, A. Fazakerley, C. J. Owen, H. Reme, and J. M. Bosqued, *Geophys. Res. Lett.* **30**(7), 1362, doi:10.1029/2002GL016411 (2003).
- <sup>44</sup>Y. Lin, X. Y. Wang, S. Lu, J. D. Perez, and Q. M. Lu, *J. Geophys. Res.* **119**, 7413, doi:10.1002/2014JA020005 (2014).
- <sup>45</sup>Y. Lin and X. Y. Wang, *J. Geophys. Res.* **110**, A12216, doi:10.1029/2005JA011243 (2005).
- <sup>46</sup>D. W. Swift, *J. Comput. Phys.* **126**, 109–121 (1996).
- <sup>47</sup>Y. Q. Hu, X. C. Guo, and C. Wang, *J. Geophys. Res.* **112**, A07215, doi:10.1029/2006JA012145 (2007).
- <sup>48</sup>M. G. Kivelson and C. T. Russell, *Introduction to Space Physics* (Cambridge University Press, Cambridge, 1995).
- <sup>49</sup>M. Øieroset, T. D. Phan, M. Fujimoto, R. P. Lin, and R. P. Lepping, *Nature* **412**(6845), 414–417 (2001).
- <sup>50</sup>A. Runov, R. Nakamura, W. Baumjohann, R. A. Treumann, T. L. Zhang, M. Volwerk, Z. Vörös, A. Balogh, K. H. Glaßmeier, B. Klecker, H. Rème, and L. Kistler, *Geophys. Res. Lett.* **30**(11), 1579, doi:10.1029/2002GL016730 (2003).
- <sup>51</sup>J. P. Eastwood, T. D. Phan, M. Oieroset, and M. A. Shay, *J. Geophys. Res.* **115**, A08215, doi:10.1029/2009JA014962 (2010).
- <sup>52</sup>K. Fujimoto, *Phys. Plasmas* **13**, 072904 (2006).
- <sup>53</sup>C. Huang, Q. Lu, Z. Yang, M. Wu, Q. Dong, and S. Wang, *Nonlinear Proc. Geophys.* **18**(5), 727–733 (2011).
- <sup>54</sup>M. H. Hong, D. W. Swift, and Y. Lin, *Adv. Space Res.* **41**, 1298–1304 (2008).
- <sup>55</sup>C. C. Chaston, J. W. Bonnell, L. Clausen, and V. Angelopoulos, *J. Geophys. Res.* **117**, A12205, doi:10.1029/2012JA018476 (2012).
- <sup>56</sup>S. Y. Huang, M. Zhou, X. H. Deng, Z. G. Yuan, Y. Pang, Q. Wei, W. Su, and Q. Q. Wang, *Ann. Geophys.* **30**, 97–107 (2012).
- <sup>57</sup>A. Runov, V. Angelopoulos, and X. Z. Zhou, *J. Geophys. Res.* **117**, A05230, doi:10.1029/2011JA017361 (2012).
- <sup>58</sup>M. M. Kuznetsova, M. Hesse, and D. Winske, *J. Geophys. Res.* **101**(A12), 27351–27373, doi:10.1029/96JA02622 (1996).
- <sup>59</sup>J. Birn, J. F. Drake, M. A. Shay, B. N. Rogers, R. E. Denton, M. Hesse, M. Kuznetsova, Z. W. Ma, A. Bhattachajee, A. Otto, and P. L. Pritchett, *J. Geophys. Res.* **106**, 3715–3719, doi:10.1029/1999JA900449 (2001).
- <sup>60</sup>H. J. Cai, D. Q. Ding, and L. C. Lee, *J. Geophys. Res.* **99**, 35–42, doi:10.1029/93JA02519 (1994).
- <sup>61</sup>M. Hesse, M. Kuznetsova, and J. Birn, *Phys. Plasmas* **11**, 5387–5397 (2004).
- <sup>62</sup>S. A. Kiehas, V. A. Angelopoulos, A. Runov, and S. S. Li, *J. Geophys. Res.* **118**, 4415–4424, doi:10.1002/jgra.50425 (2013).
- <sup>63</sup>S. A. Kiehas, V. A. Angelopoulos, A. Runov, M. B. Moldwin, and C. Möstl, *J. Geophys. Res.* **117**, A05231, doi:10.1029/2011JA017377 (2012).
- <sup>64</sup>L. A. Frank, W. R. Paterson, J. B. Sigwarth, and S. Kokubun, *J. Geophys. Res.* **105**(A7), 15897–15912, doi:10.1029/1999JA000439 (2000).
- <sup>65</sup>H. Nakai and Y. Kamide, *J. Geophys. Res.* **105**(A8), 18781–18792, doi:10.1029/2000JA900044 (2000).